

Nuclear and Electron Spin Resonance Studies on Skyrmion-Hosting Lacunar Spinels

Markus Prinz-Zwick, Bertalan G. Szigeti, Thomas Gimpel, Dieter Ehlers, Vladimir Tsurkan, Andrey O. Leonov, Björn Miksch, Marc Scheffler, Ioannis Stasinopoulos, Dirk Grundler, István Kézsmárki, Norbert Büttgen, and Hans-Albrecht Krug von Nidda*

Magnetic resonance techniques at nuclei and electrons are applied to characterize the electronic structure and collective magnetic excitations throughout the magnetic phase diagrams of the lacunar spinels GaV_4S_8 and GaV_4Se_8 showing cycloidal, Néel-type skyrmion lattice and ferromagnetically polarized phases. ^{71}Ga nuclear magnetic resonance (NMR) provides a local probe of the rhombohedral distortion and the resulting uniaxial magnetic anisotropy via the detection of electric field gradients (EFGs) and hyperfine coupling at the gallium sites of these lacunar spinels. Broadband electron spin resonance (ESR) allows identifying clockwise, counterclockwise, and breathing modes of the skyrmion-lattice phase supported by theoretical simulations.

1. Introduction

Stoichiometric chalcogenides and halides displaying fractional formal valence states for the metallic species are also referred to as mixed-valence systems. In such compounds, one electron (or electronic hole) is formally shared between two or among more metal sites. In the solid-state context, a wide variety of intriguing phenomena is encountered in mixed-valence materials, ranging from charge ordering in, e.g., manganates^[1,2] and vanadates,^[3,4] to heavy-fermion behavior in LiV_4O_4 ^[5,6] and a possible spin-liquid phase in $\text{Ba}_3\text{InIr}_2\text{O}_9$,^[7,8] where the latter phenomena are accompanied by strong magnetic frustration. Mixed valence often implies lattice configurations featuring well-

defined and clearly separated dimers or M_p clusters ($p = 2, 3, 4, \dots$, corresponding to dimers, trimers, tetramers, and so on) of transition-metal ions. With $n \cdot p + 1$ electrons associated with such a unit, where n valence electrons reside at each transition-metal ion and the additional “+1” electron may be delocalized over a molecular-like, extended orbital state.^[9] Whether the net cluster spin is given only by this “single” electron or also by other d electrons depends on specific details of each particular system, such as the actual n and p values, covalency effects, and strength of Hund’s coupling. The distributed elec-

tronic state within a cluster may exhibit instabilities towards symmetry breaking and “local” charge disproportionation. Certain anisotropies would be then present as concerns the “local” charge distribution. This degree of “instability” is related as well to collective, intercluster couplings. The latter give rise to collective ordering phenomena such as cooperative Jahn–Teller distortions and/or magnetic ordering.

The so-called lacunar spinels GaM_4X_8 , with $M = \text{V}, \text{Mo}$ and $X = \text{S}, \text{Se}$, represent a class of compounds where such behavior has been observed experimentally.^[10–15] Here, charge instability within M_4X_4 cubanes in the cubic parent crystal structure can drive structural transitions to low-temperature polar rhombohedral^[16,17] or antipolar orthorhombic^[18,19] phases. In systems with

M. Prinz-Zwick, B. G. Szigeti, T. Gimpel, D. Ehlers, V. Tsurkan, I. Kézsmárki, N. Büttgen, H.-A. Krug von Nidda
Experimental Physics V
Center for Electronic Correlations and Magnetism
Institute of Physics
University of Augsburg
D-86135 Augsburg, Germany
E-mail: hans-albrecht.krug@physik.uni-augsburg.de

A. O. Leonov
Chirality Research Center
Hiroshima University
Higashi-Hiroshima, Hiroshima 739-8526, Japan

B. Miksch, M. Scheffler
1. Physikalisches Institut
Universität Stuttgart
Pfaffenwaldring 57, 70569 Stuttgart, Germany

I. Stasinopoulos
Physik Department E10
Technische Universität München
85748 Garching, Germany

D. Grundler
Laboratory of Nanoscale Magnetic Materials and Magnonics
Institute of Materials (IMX)
École Polytechnique Fédérale de Lausanne (EPFL)
1015 Lausanne, Switzerland

 The ORCID identification number(s) for the author(s) of this article can be found under <https://doi.org/10.1002/pssb.202100170>.

© 2021 The Authors. physica status solidi (b) basic solid state physics published by Wiley-VCH GmbH. This is an open access article under the terms of the Creative Commons Attribution License, which permits use, distribution and reproduction in any medium, provided the original work is properly cited.

DOI: 10.1002/pssb.202100170

rhombohedral low-temperature state, such as GaV_4S_8 and GaV_4Se_8 , an apparently robust Dzyaloshinskii–Moriya (DM) exchange allows then the stabilization of magnetic skyrmion states and field-driven condensed skyrmion lattices (SkLs).^[11] The peculiar magnetoelectric properties featured by these systems offer unique new functionalities, owing to the distinctive type-I multiferroic nature of the compounds, where the magnetically ordered states can be simultaneously ferroelectric and ferroelastic as well. These ferroic properties do not only coexist but can be also coupled.^[12] Such couplings can lead to textured multiferroic states. In this respect, the magnetoelectric lacunar spinels are remarkably different as compared with the extensively studied cuprate Cu_2OSeO_3 , which is a magnetoelectrically coupled chiral cubic helimagnet.^[20,21] From the theoretical point of view the electronic structure in case of fractional occupation within the M_4X_8 cubanes is still an open question.^[22] Standard density functional theory (DFT) calculations are not sufficient to account for the experimentally observed bandgap, and a more sophisticated DFT assessing the performance of various exchange-correlation potentials could not be supported by optical spectroscopy experiments,^[23] recently.

In the present study, we focus on the local electronic properties of the lacunar spinels GaV_4S_8 and GaV_4Se_8 from the magnetic resonance point of view both at gallium nuclei and vanadium electrons. Previously, we have analyzed the magnetic anisotropy by means of angular dependent ferromagnetic resonance (FMR) measurements at Q-band frequency in the ferromagnetically polarized regime.^[13,24] Moreover, broadband electron spin resonance (ESR) allowed identifying the characteristic collective modes of the SkL phase, i.e., clockwise, counterclockwise, and breathing mode in GaV_4S_8 .^[25] Here, we will give a comprehensive ESR and nuclear magnetic resonance (NMR) study of the entire phase diagram probing the local environment of electron and nuclear spins.

2. Sample Characterization

Single crystals of GaV_4S_8 and GaV_4Se_8 have been prepared by chemical transport reaction using iodine as transport agent as described previously.^[11,13] Magnetic phase diagrams have been derived from magnetization, magnetic torque, specific heat, small-angle neutron scattering, as well as atomic force microscopy measurements. Upon cooling both noncentrosymmetric cubic systems (T_d point symmetry) undergo a Jahn–Teller transition into a rhombohedrally distorted (C_{3v} point symmetry) polar structural phase at about 44 and 42 K followed by cycloidal magnetic order below 13 and 18 K for the sulfide and the selenide compound, respectively.^[26,27] Due to the trigonal Jahn–Teller distortion along the $\langle 111 \rangle$ axes, four structural domains emerge which explains coexisting phases for orientations of the magnetic field $H \parallel \langle 111 \rangle$ and $H \parallel \langle 110 \rangle$. Only for $H \parallel \langle 100 \rangle$ all domains are equivalent, as we prove in the next section.

Note that, in the lacunar spinels belonging to the C_{nv} symmetry class, in contrast to cubic helimagnets like MnSi , no Lifshitz invariants are present along the high-symmetry z axis. Therefore, in these compounds, only modulated magnetic structures with wavevectors perpendicular to the field (i.e., skyrmions and helioids) are favored by the DM interaction, but the conical phase,

which is considered as a main rival of skyrmions, is suppressed. Nevertheless, theoretical considerations have shown that the anisotropy plays an important role for the stability of the Néel-type skyrmion phase.^[28]

The important difference of both compounds is the sign of the uniaxial anisotropy within the Jahn–Teller phase, which is of easy axis type for GaV_4S_8 , but easy plane for GaV_4Se_8 . In zero magnetic field, both compounds exhibit a cycloidal (Cyc) magnetic ground state, which for the magnetic field applied along the $\langle 111 \rangle$ directions on increasing magnetic field transforms at first into a SkL phase and then into a ferromagnetically (FM) polarized phase. While in GaV_4S_8 , the increase in the easy-axis anisotropy to low temperatures suppresses both SkL and Cyc phases below 5 K, the easy-plane anisotropy stabilizes both phases down to zero temperature in GaV_4Se_8 . Moreover, it is important to note that in GaV_4S_8 , the SkL phase is observed for $H \parallel \langle 111 \rangle$ and $H \parallel \langle 100 \rangle$ for all domains, but in case of $H \parallel \langle 110 \rangle$ only for those domains which span an angle of 35° with the static field, but not for those which are orthogonal to the field.^[11,25] In GaV_4Se_8 , no SkL phase is observed for $H \parallel \langle 100 \rangle$, but for $H \parallel \langle 111 \rangle$, the SkL phase shows up down to lowest temperatures for the domains with the rhombohedral axis parallel to the static field. For $H \parallel \langle 110 \rangle$ in the domains with the rhombohedral axis spanning an angle of at 35° with the magnetic field, the SkL phase appears in a certain temperature range below T_C . For all other domains, the Cyc phase—although showing up down to lowest temperatures—directly transforms into the FM phase on increasing field.^[29] This is in agreement with Dzyaloshinskii’s solution that the spiral state gradually increases its period and expands into the homogeneous state.

3. Nuclear Magnetic Resonance

We perform NMR at the gallium nuclei (with gyromagnetic ratio $^71\gamma/2\pi = 13.021 \text{ MHz/T}$ of ^71Ga) at an irradiation frequency of $\omega/2\pi = 40 \text{ MHz}$, which corresponds to applied magnetic fields H of $\mu_0 H \approx 3 \text{ T}$. **Figure 1** shows the temperature dependence of ^71Ga spectra from the paramagnetic phase down to the magnetically ordered state. In the paramagnetic phase with cubic crystallographic symmetry, the spectral pattern consists of a single unsplit spectral line, as exemplified by the spectrum recorded at 50 K. Around the Jahn–Teller transition at $T_{JT} = 44 \text{ K}$, the reduction of the site symmetry from cubic to rhombohedral yields a distortion of the cubic cell along one of the body diagonals $\langle 111 \rangle$, and, consequently, the line splits due to the emergence of an electric field gradient (EFG) at the gallium sites. The interaction between the electric quadrupole moment of the Ga nuclei with nuclear spin $I = 3/2$ and the EFG of surrounding charges splits the signal into a central line and two satellites, where the distance of the satellite lines depends on the orientation of the principal axes of the EFG tensor with respect to the direction of the externally applied magnetic field H . Please note that, in the magnetic-field region investigated here, the electronic magnetization is saturated and points along the applied field, irrespective of its orientation. As the orientation of the EFG is different for Ga nuclei located in different rhombohedral domains for a general field direction, we expect a central line accompanied by several pairs of satellites

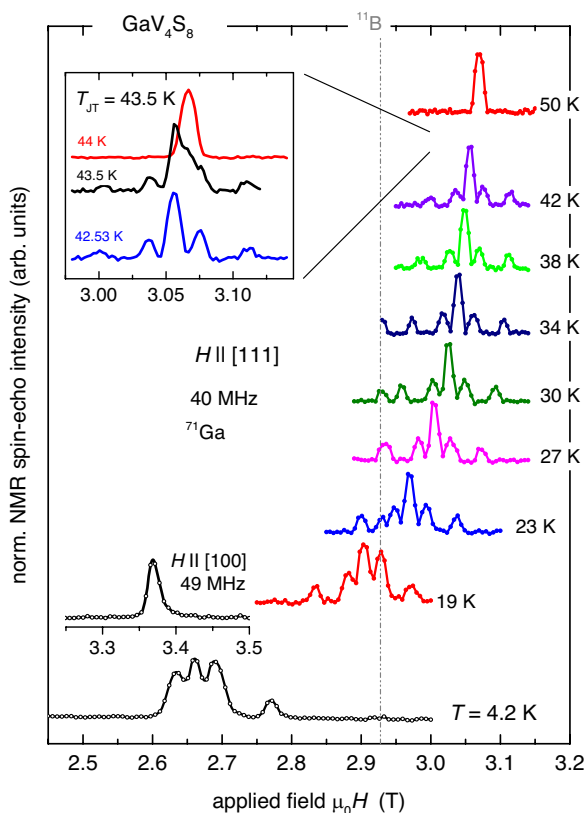


Figure 1. Temperature dependence of ^{71}Ga NMR spectra in GaV_4S_8 . Below the Jahn–Teller transition at $T_{\text{JT}} = 43.5\text{ K}$, the deformation of the GaS_4 clusters yields electric field gradients which split the single-line spectrum observed for $T < T_{\text{JT}}$ into several lines. At $\mu_0 H = 2.93\text{ T}$, an additional line from boron ^{11}B is an artifact related to details of the experimental setup. Upper inset: magnification of the temperature range $42.53 < T < 44\text{ K}$ around the Jahn–Teller transition. Lower inset: spectrum for $H||[100]$ at $T = 4.2\text{ K} < T_{\text{C}}$, where the condition of the “magic angle” is fulfilled for all domain contributions simultaneously, resulting in a single, solitary spectral line.

as observed for $H||[111]$ in Figure 1 below T_{JT} . For the so called “magic angle” (54.7°) between the direction of the EFG and the direction of the externally applied magnetic field H , the interaction between the nuclear quadrupole moment and the surrounding EFG vanishes and the split spectral pattern collapses into one single, solitary spectral line. Such situation is documented in the lower inset of Figure 1 for $H||[100]$ at 4.2 K , where the distortion axes of all domains span the “magic angle” with the externally applied field H , resulting in the single, solitary line observed.

A closer inspection of the orientation $H||[111]$ is displayed in Figure 2, where the simulation of the spectra (green solid line) comprises two quadrupole–split patterns due to the coexistence of four different rhombohedral domains:^[11] one domain with its magnetic easy axis oriented parallel to the applied field H along $[111]$ (red dotted line, 0°), whereas each easy axis of the other three domains all span 71° with $H||[111]$ (blue dashed line). In the magnetically ordered state, below $T_{\text{C}} = 13\text{ K}$, the internal magnetic field shows a difference of 40 mT between the unique domain and the other three domains (cf. Figure 2, bottom

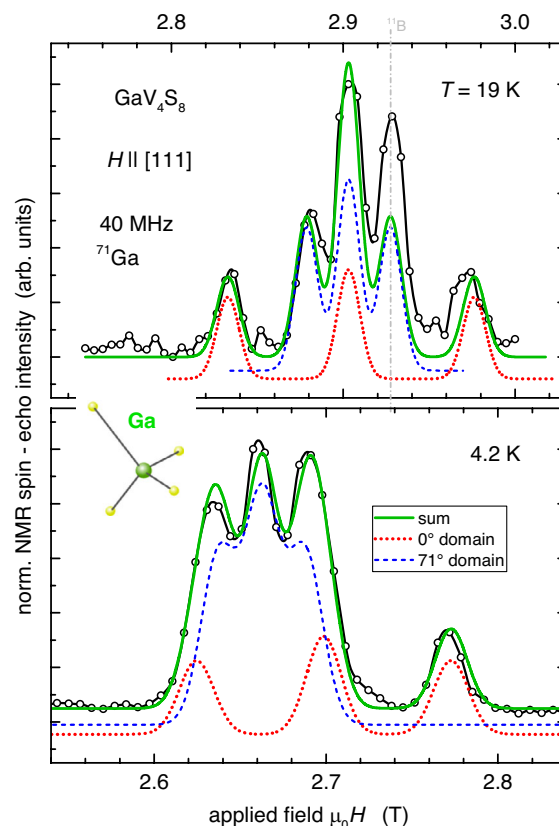


Figure 2. ^{71}Ga NMR spectra (black open circles) for the rhombohedral phase below the Jahn–Teller transition at $T = 19\text{ K} > T_{\text{C}}$ (upper frame) and within the magnetically ordered state at $T = 4.2\text{ K} < T_{\text{C}}$ (lower frame), respectively. The dashed and dotted lines are simulations for quadrupole splittings of different contributions from several crystal domains, added together (green solid line). Note that, at 19 K , the discrepancy visible at 2.93 T is due to the ^{11}B line.

frame), as it is unambiguously observed due to the shift between the central lines. Here, the coincidence of the central lines observed for the different domains at elevated temperatures $T_{\text{C}} < T < T_{\text{JT}}$ is lifted-up, as a consequence of the rhombohedral anisotropy of the hyperfine coupling tensor at the gallium sites. From our simulations, we deduce the major component V_{zz} of the axially symmetric EFG tensor at the Ga site $V_{zz} = 7.27 \times 10^{20}\text{ V m}^{-2}$.

Figure 3 shows the temperature dependence of the EFG formation deduced from our NMR experiments toward decreasing temperatures, which concomitantly evolves with the temperature-dependent dielectric polarization P as determined from pyrocurrent measurements performed on a (111) -plane contacted GaV_4S_8 single crystal in a Quantum Design PPMS. Such behavior is well known in case of ferro- or antiferroelectric phase transitions,^[30] which allows for the investigation of structural distortions from a local point of view, irrespective of different domain orientations which always have to be taken into account probing the bulk. From the temperature-dependent line shift K of the spectra in Figure 1, we determine the hyperfine coupling constant A_{hf} via the relation $K = A_{\text{hf}} \cdot \chi + K_0$, where χ is the bulk susceptibility obtained from

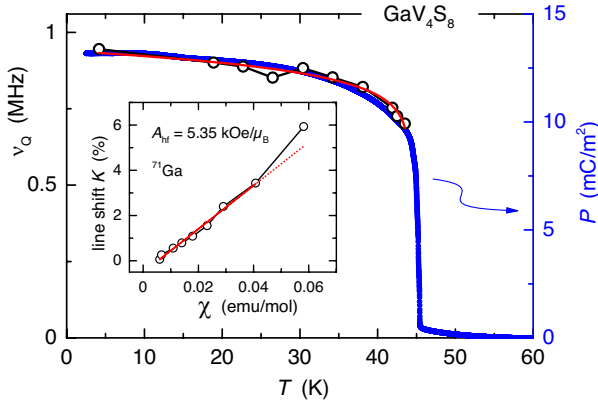


Figure 3. Temperature dependence of the quadrupole frequency ν_Q of the ^{71}Ga nuclei (open circles, left axis) and of the dielectric polarization P in GaV_4S_8 (blue data, right axis). The red line is a fit to the temperature-dependent quadrupole coupling $\nu_Q \cdot (1 - T/T_J)^{\beta}$ for GaV_4S_8 ($T_J = 44$ K), where $\beta = 0.07$ and $\nu_Q = 0.94$ MHz. Inset: Jaccarino–Clogston plot yields the hyperfine coupling constant $A_{\text{hf}} = 5.35$ kOe/ μ_B of the gallium isotope.

a SQUID-measurement in a Quantum Design MPMS5 magnetometer and K_0 is the temperature-independent chemical shift. This relation correlates the electronic spin susceptibility and the line shift with temperature T as an implicit parameter and gives the nuclear hyperfine field in terms of Bohr magnetons.^[31] A fit in the paramagnetic temperature range $23 < T < 50$ K gives the value $A_{\text{hf}} = 5.35$ kOe/ μ_B (cf. red solid line in the inset of Figure 3).

4. Model Calculations of Collective Magnetic Excitations

Previously, we have discussed the magnetic resonance modes observed in Cyc, Néel-type SkL, and FM phases of GaV_4S_8 ^[25] from an experimental point of view and in analogy to the modes reported from helical, Bloch-type skyrmion, and conical phases in MnSi ^[32,33] and Cu_2OSeO_3 . We identified the three characteristic resonance modes known from Bloch-type SkLs, i.e., clockwise (CW), counterclockwise (CCW), and breathing (BR) mode, in the Néel-type SkL as well. In the following, we refine our analysis based on a rigorous theoretical treatment of the spin dynamics in GaV_4S_8 .

Before we will discuss the results of our ESR experiments, it is instructive to present model calculations of the resonant excitations in the different magnetic phases of lacunar spinels. For the theoretical description of the magnetic resonance modes, we start from the energy density functional for a noncentrosymmetric ferromagnet with symmetry C_{nv} consisting of contributions from symmetric exchange, DM interaction, Zeeman energy, and uniaxial anisotropy attributed to the low-temperature Jahn–Teller distorted rhombohedral crystal structure, given by

$$w = \sum_{i,j} \left(\frac{\partial m_j}{\partial x_i} \right)^2 + L_{xz}^{(x)} + L_{yz}^{(y)} - \mathbf{m} \cdot \mathbf{h} - k_u m_z^2 \quad (1)$$

Here, the space coordinates x are measured in units of the characteristic length $L = A/D$ of the modulated spin structure, where A and D denote the exchange stiffness and DM constant, respectively. In these units, the spiral period in zero magnetic field and zero anisotropy equals $\lambda = 4\pi L$. The Cartesian coordinate system is defined such that the plane of the SkL coincides with the xy plane and the skyrmion cores are coaligned with the z direction, i.e., the $[111]$ axis of rhombohedral distortion. $\mathbf{m} = \mathbf{M}/M$ is the normalized magnetization and $\mathbf{h} = \mathbf{H}/H_0$ the magnetic field with $H_0 = D^2/AM$. The uniaxial anisotropy constant $k_u = K_u M^2 A/D^2$ is adapted correspondingly. The Lifshitz invariants for the given crystal symmetry read

$$L_{xz}^{(x)} = m_x \left(\frac{\partial m_z}{\partial x} \right) - m_z \left(\frac{\partial m_x}{\partial x} \right) \quad (2)$$

and analogously $L_{yz}^{(y)}$, which confine the propagation vector of the modulated states, i.e., cycloids or skyrmions, to the xy plane. As in the lacunar spinels under consideration, L is not very large as compared with the distance of neighboring spins, it is necessary to consider a discrete variant of the above model with classical spins \mathbf{S}_i normalized to unit length $S = 1$ on a square-lattice following ref. [34]. The energy-density functional then reads

$$w = \sum_{\langle i,j \rangle} \mathbf{S}_i \cdot \mathbf{S}_j - \sum_i [\mathbf{h} \cdot \mathbf{S}_i + k_u (\mathbf{S}_i \cdot \mathbf{n})^2] - \frac{J}{D} \sum_i [(\mathbf{S}_i \cdot \hat{\mathbf{y}}_{i+\hat{x}}) \cdot \hat{\mathbf{y}} - (\mathbf{S}_i \cdot \hat{\mathbf{x}}_{i+\hat{y}}) \cdot \hat{\mathbf{x}}] \quad (3)$$

with $\mathbf{h} = \mathbf{H}J/D^2$ and $k_u = K_u J/D^2$. The sum $\langle i,j \rangle$ runs over nearest neighbors. $\hat{\mathbf{x}}$, $\hat{\mathbf{y}}$, and \mathbf{n} denote unit vectors along x and y directions, and the rhombohedral axis, respectively.

The dynamics was investigated following ref. [35] with the additional possibility of oblique magnetic fields.^[28] This option gives an important insight, since the Néel skyrmions do not co-align with the external magnetic field but stay confined to the direction to the axis of anisotropy, the rhombohedral axis in the present case, in strong contrast to cubic skyrmion hosts. First of all, a starting spin configuration close to the global optimum was found by simulated cooling and improved via relaxation by Landau–Lifshitz–Gilbert (LLG) equation. Then an oscillating magnetic field was added and, again based on LLG equation, the imaginary part of the dynamic susceptibility was numerically calculated using the fourth-order Runge–Kutta method.

In the Cyc phase, as shown in Figure 4, one obtains two resonance modes, which are degenerate for the isotropic case, but split linearly on increasing uniaxial anisotropy k_u . From the frequency ratio of 3:1, which corresponds to the Cyc modes (15 and 5 GHz) observed in GaV_4S_8 at 11 K,^[25] we obtain the anisotropy constant $k_u = 0.37$. This value is used for further simulations of the magnetic-field dependence of the resonance spectra based on the LLG equation. Figure 5a shows the evolution for the magnetic field applied along one of the $\langle 100 \rangle$ directions, which span an angle of 54.7° with respect to each of the four possible easy $\langle 111 \rangle$ axes of rhombohedral distortion, i.e., the effective field is the same in all four domains.

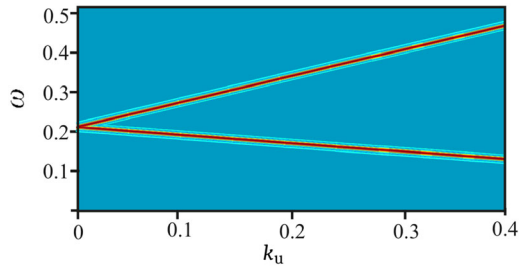


Figure 4. Color-coded plot of the normalized eigenfrequencies $\omega = \Omega_j/D^2$ of the resonant modes in the Cyc phase dependent on the strength of uniaxial anisotropy k_u . Turquoise blue color defines the zero level, whereas red color indicates maximum absorption.

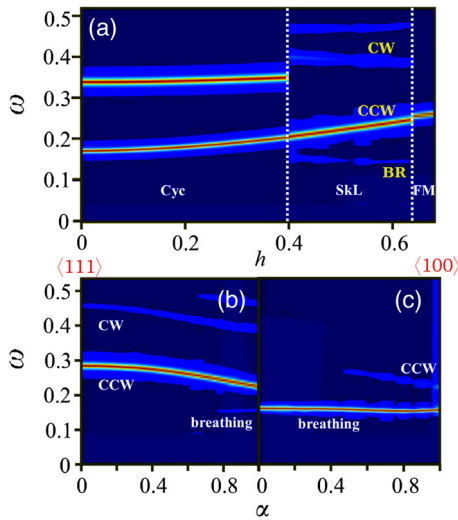


Figure 5. Color-coded plots of microwave absorption dependent on magnetic field h and angle α between h and skyrmion axis $\langle 111 \rangle$ for $k_u = 0.37$: dark blue color defines the zero level, whereas red color indicates maximum absorption. Upper frame (a): Field dependence of the normalized frequencies $\omega = \Omega_j/D^2$ of resonant modes in Cyc, SkL, and FM phase for the static magnetic field applied along the $\langle 100 \rangle$ axis (i.e., $\alpha = 0.95 = 54.7^\circ$). Lower frame: Dependence of the skyrmion modes on the angle α for the magnetic microwave field applied b) perpendicular and c) parallel to the static magnetic field chosen as $h = 0.6$, respectively.

Starting from $h = 0$, the Cyc modes are only slightly dependent on the magnetic field in the range $h < 0.4$, but reveal a significant change when entering the SkL phase. While the lower (CCW) mode continues to increase with the field, the upper (CW) mode exhibits a discontinuous shift to higher frequency and its intensity weakens. Moreover, a third mode, i.e., the BR mode, appears below the lower mode. Notably, above the CW mode another weak excitation shows up. The calculated branches in the SkL phase of Figure 5a substantiate the original conclusion drawn from the field dependence of experimentally detected resonances in ref. [25] that the energetic hierarchy of BR, CCW, and CW in GaV_4S_8 is different from the hierarchy CCW, BR, and CW in the previously studied chiral magnet Cu_2OSeO_3 . Finally, in the ferromagnetic phase one obtains the classical FMR attributed to uniform spin precession.

It is also instructive to model the SkL modes dependent on the angle between the external magnetic field and the easy axis. Figure 5b shows the decrease in the eigenfrequencies of CW and CCW mode with increasing declination of the magnetic field from the $\langle 111 \rangle$ axis for angles up to 54.7° , corresponding to the $\langle 100 \rangle$ direction. The BR mode and the excitation above the CW mode appear only for angles larger than 35° . While in panel (b), the magnetic microwave field is applied perpendicular to the static magnetic field, it is oriented parallel to the static field in the frame (c). Here, the angular-independent breathing mode dominates for all static-field directions, whereas the CCW mode appears only for angles above 25° and the CW mode remains invisible at all.

5. Electron Spin Resonance

Broadband ESR spectroscopy was performed by means of inductive coupling of the sample to microwave fields of variable frequency between 10 MHz and 35 GHz above a coplanar waveguide (CPW) within a given external static magnetic field. A network analyzer recorded the transmission of the microwave through the CPW in terms of the amplitude of the scattering parameter $|S_{12}|$. To reduce field-independent microwave responses in the setup, all spectra shown here are difference spectra $\Delta|S_{12}(\nu)|$ obtained after subtraction of an appropriate reference spectrum. Further details can be found in refs. [32,36]. For the data shown in Figure 6 and 7, the signal line was $20\ \mu\text{m}$ wide, i.e., smaller than the diameter of the plate-like samples of about 1 mm. Such an approach allows to detect modes of CW, CCW, and BR character, as the microwave magnetic field provides field components parallel and perpendicular to the applied magnetic field. The external static field was applied perpendicular to the CPW plane. As reference we subtracted the spectrum $|S_{12}^{\text{ref}}(\nu)|$ taken at 2 T from the recorded spectra $|S_{12}(\nu)|$.^[32] In case of the measurements illustrated in Figure 8 and 9, the CPW center conductor was $100\ \mu\text{m}$ wide, the external static field was applied within the CPW plane, and as reference spectrum, we used the median of all spectra of a given experimental series.^[36]

Figure 6 illustrates the evolution of the frequency-dependent ESR spectra in GaV_4S_8 on passing all three phases from the Cyc, through the SkL into the FM-polarized phase at $T = 12\ \text{K}$ for the magnetic field applied along the $[001]$ direction, where all domains yield equivalent signals. The observed resonances have been fitted by asymmetric Lorentzian lines accounting for some contribution α of dispersion to the absorption signal as given by

$$P(\nu) = \frac{I_{\text{ESR}}[\Delta\nu + \alpha(\nu - \nu_0)]}{(\nu - \nu_0)^2 + \Delta\nu^2} \quad (4)$$

Here I_{ESR} , ν_0 , and $\Delta\nu$ denote the intensity, resonance frequency, and line width, respectively. The nonzero dispersion to absorption ratio α , which in the present case exhibits values $\alpha < 0.2$, arises for reasons of the excitation and detection geometry of the CPW. In the Cyc phase for $0 \leq H \leq 600\ \text{Oe}$, the low-frequency resonance is well described by a single Lorentzian 1, whereas the high-field resonance is rather represented by the sum of two Lorentzians 2 + 3. On entering the SkL phase at

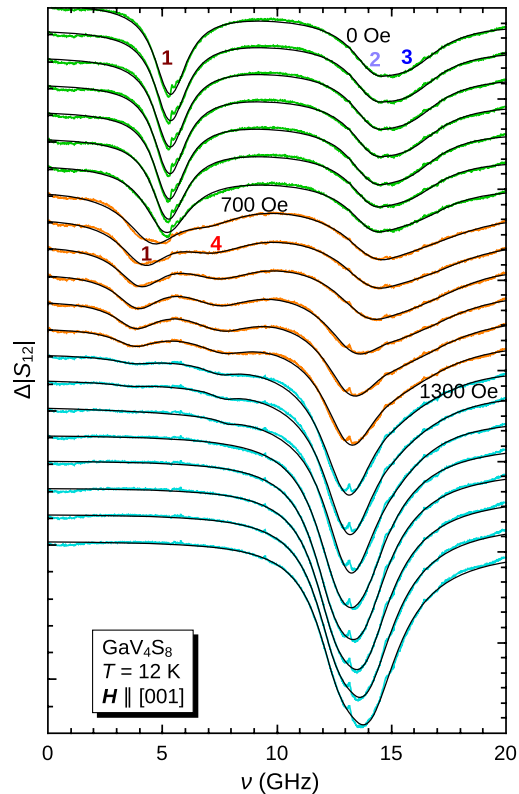


Figure 6. Broadband microwave transmission spectra $|S_{12}|$ of GaV_4S_8 taken at $T = 12\text{ K}$ for different magnetic fields applied along the cubic $[001]$ direction in Cyc (green), SkL (orange), and FM (blue) phases. Black solid lines represent fits by Lorentzian lines as described in the text.

$H = 700\text{ Oe}$, line 4, also well described by a single Lorentzian, separates from line 1. Both lines remain present throughout the SkL phase but fade out on entering the FM phase above 1300 Oe . In contrast, lines 2 and 3 strengthen on passing the SkL phase and become dominant in the FM phase.

The fitting results are depicted in Figure 7. Within the Cyc phase both the low-frequency and high-frequency resonances show up at frequencies 5.2 and $14.2/15.8\text{ GHz}$, respectively, with approximately field-independent intensities. This is basically in agreement with the simulations Figure 5a, where, although the additional splitting of the upper line is not resolved, the upper line at least turns out to be broader than the lower line. Returning to the experimental data in Figure 7, at the transition into the SkL phase the two upper lines slightly shift, while the lower mode splits into two lines at about 4 and 7 GHz . Indeed the simulation in Figure 5a nicely reproduces the splitting of the lower mode and even resolves the splitting of the upper mode. Concerning the intensities of the experimental data, the two upper lines dominate, whereas the two lower lines continuously weaken on increasing field and their intensities approach zero at 1500 Oe . Here, a direct comparison with the simulations is not conclusive, as the excitation geometry of the CPW produces a coherent mixture of transverse and longitudinal microwave fields. Finally, in the FM phase the intensity of line 2 linearly increases on increasing field, while line 3 crosses to slightly lower

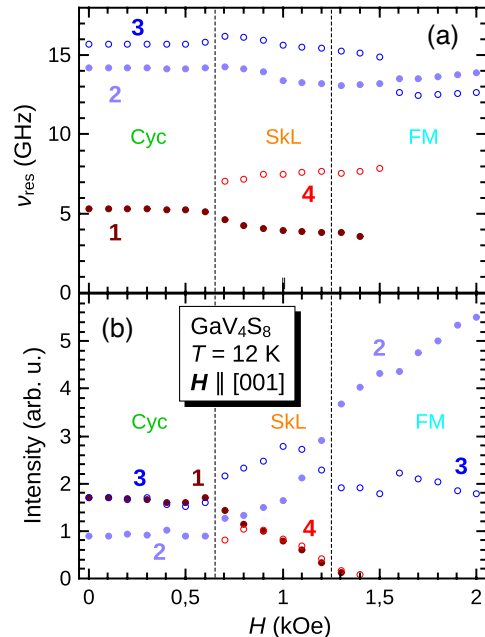


Figure 7. Field dependence of a) the frequencies of resonant modes of GaV_4S_8 in Cyc, SkL, and FM phase and b) corresponding intensities as obtained from the fitting of the spectra shown in Figure 6. Note that, lines 2 and 3 can be unequivocally separated throughout the whole field regime: at the crossing of the intensities at $H = 1.2\text{ kOe}$, the resonance fields are well separated and at the crossing of the resonance frequencies at $H = 1.6\text{ kOe}$, the lines can be distinguished by their intensities.

frequency and practically merges with line 2. Although the simulations predict a quite continuous transformation of the lower Cyc mode 1 via the CCW mode 4 into the ferromagnetic resonance 2, the experiment rather suggests a continuation of line 2 through all three phases. However, so far the simulations did not take into account possible anisotropic g values and demagnetization effects due to the sample shape, which are essential for a fully realistic modeling of the data.

Nevertheless, our present state of the analysis successfully describes the observed collective excitations in the SkL of GaV_4S_8 . Especially, the coexistence of two lines close to 15 GHz is established and also in agreement with the theoretical simulations, which predict such a pattern for the SkL phase in oblique fields on approaching the $\langle 100 \rangle$ directions. For $H||[111]$ and $H||[110]$, a splitting of the upper mode could not be resolved. Detailed frequency-field diagrams for those orientations have been shown in ref. [25]. While for $H||[111]$ Cyc and SkL phases of the easy domain and the three other domains, which are tilted by 70.5° , can be simultaneously observed and well resolved, in case of $H||[110]$, only the two domains tilted by 35.3° host a SkL. But for the other two domains with the easy axes perpendicular to the field, the Cyc phase directly transforms into the FM phase. This transition we want to trace in more detail now.

Figure 8 shows color-coded plots of microwave absorption spectra of GaV_4S_8 dependent on magnetic field and frequency at different temperatures for the magnetic field applied along the $[110]$ direction. At $T = 2\text{ K}$, the ferromagnetic resonance starting from 22 GHz at $H = 0$ splits into two branches. One of them,

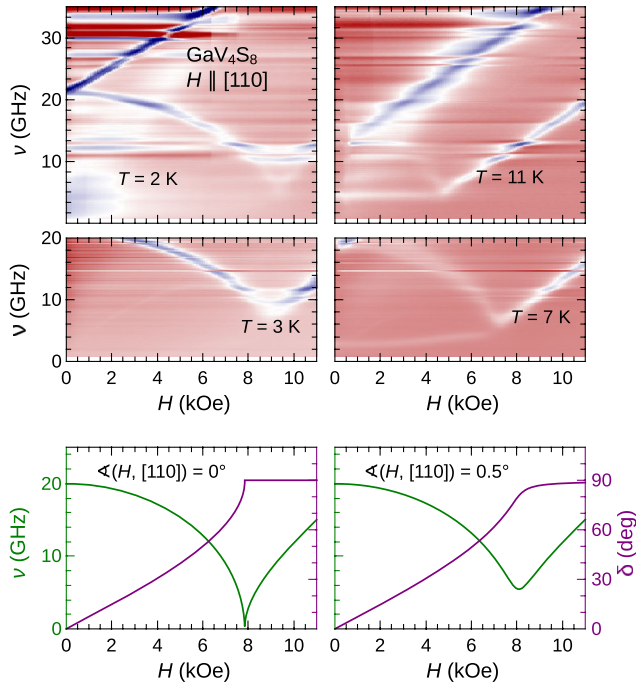


Figure 8. Color-coded plots of the transmission spectra $|S_{12}|$ of GaV_4S_8 in the frequency versus magnetic field plane at different temperatures for the field applied along the cubic [110] direction (red: zero level, blue: strong absorption, the intermediate white color has been shifted to emphasize weak amplitudes). The bottom frames display the field dependence of the ferromagnetic resonance frequency (green) and the equilibrium angle δ of the magnetization (purple) for the magnetic field applied perpendicular to the easy [111] axis and a small misalignment of 0.5° , respectively. Field-independent signatures in the four upper panels are attributed to resonances in the CPW and microwave cables.

which can be ascribed to the domains with their easy [111] axis spanning an angle of 35.3° with the magnetic field, increases linearly with the field. The other one arising from the domains, for which the easy [111] axis spans an angle of 90° with the magnetic field, decreases with negative curvature, takes a minimum at about 9 kOe, and increases again approaching a linear dependence for higher fields. Note that, the weaker broad low-frequency absorption at fields below 3 kOe is an artifact of the used CPW. The spectra taken at $T = 3$ K with another CPW working only up to 20 GHz does not reveal this artifact in that field-frequency range. At $T = 7$ K, the domains with the easy axis oriented at 90° clearly show the low-frequency Cyc mode at 3 GHz persisting up to 7 kOe, where it meets the down turning resonance branch on the transition into the ferromagnetically polarized phase. No SkL phase shows up for these domains as documented by the spectra at $T = 11$ K. Cyc and SkL phases of the domains with the easy axis oriented at 35.3° , which show up at fields below 1 kOe, cannot be resolved here due to the coarse field scale.

The ferromagnetic resonance for the domains with the easy axis close to the external field follows a linear dependence, while for the domains with the field applied perpendicular to the easy axis, the field dependence of the eigenfrequency exhibits a non-monotonous field dependence. This can be numerically simulated based on the Smit–Suhl formula^[37]

$$\left(M \sin \theta \cdot \frac{\omega}{\gamma}\right)^2 = \frac{\partial^2 F}{\partial \theta^2} \frac{\partial^2 F}{\partial \varphi^2} - \left(\frac{\partial^2 F}{\partial \theta \partial \varphi}\right)^2 \quad (5)$$

with the free energy F consisting of the sum of Zeeman energy $F_{\text{Zee}} = -\mathbf{M} \cdot \mathbf{H}$, of the magnetization M in the magnetic field H , the demagnetization $F_{\text{dem}} = \mathbf{M} \mathbf{N} \mathbf{M}$ with the demagnetization tensor \mathbf{N} , resulting from the shape of the sample, and uniaxial anisotropy energy $F_{\text{ani}} = -K_u \sin^2 \delta$, where δ denotes the angle between [111] axis and magnetization M . In our case, the sample is a thin disk within the (110) plane. The orientation of the magnetization is defined by the angles θ and φ , which denote the polar angle with respect to the normal of the disk plane and the azimuth angle with respect to the [100] axis, respectively. The orientation of the magnetic field is given analogously by θ_H and φ_H . Minimization of the free energy yields the equilibrium angle δ of the magnetization with respect to the easy axis and the corresponding resonance frequency for a given magnetic field.

The lower left frame of Figure 8 shows the result of the calculations. As long as the external field is smaller than the anisotropy field the magnetization is gradually rotated from the [111] axis ($\delta = 0^\circ$) to the direction of the magnetic field ($\delta = 90^\circ$). In this case, the resonance frequency decreases down to zero until the magnetization is parallel to the external field. Below the anisotropy field the resonance corresponds to the not-aligned FMR mode, whereas for fields above the anisotropy field the scenario of the aligned mode is reached and its frequency increases with the applied field. To observe this downturn to exactly zero frequency demands a very accurate orientation of the sample. The lower right frame shows the calculated field dependence of the eigenfrequency for a slight misalignment of 0.5° , only. In this case, the minimum eigenfrequency is already significantly larger than zero. These calculations nicely match the experimentally observed field dependence of the ferromagnetic resonance on passing from the not-aligned to aligned FMR mode.

In GaV_4Se_8 , the easy-plane anisotropy gives rise to a different behavior, as illustrated in Figure 9. This is best documented by the spectra obtained for $H \parallel [111]$ on the left-hand side of Figure 9, i.e., \mathbf{H} is applied along the hard axis. For all temperatures, the zero-field spectra exhibit the two resonance modes characteristic of the Cyc phase. At $T = 4$ K, they reside at 6 and 12.5 GHz. At $T = 10$ K, the corresponding resonance frequencies are slightly smaller. The frequency of the upper mode decreases significantly on increasing field, whereas the frequency of the lower mode increases only slightly until both modes unite at about $H_C^{71} = 1.5$ kOe. At this field value, the three domains with the hard axis spanning an angle of 71° with the magnetic field, undergo the phase transition into the FM-polarized phase. The frequency of the united FMR increases linearly on further increasing field. Moreover, a new resonance with a frequency of 2.5 GHz appears close to $H_{C1}^0 = 1$ kOe, at the transition from the Cyc into the SkL phase of the remaining domain with the hard axis parallel to the field. Its frequency varies slightly up to $H_{C2}^0 = 4$ kOe, where the transition into the FM phase takes place. To higher fields, the corresponding FMR frequency increases with a slope comparable to the main resonance of the three other domains. Thus, the mode at

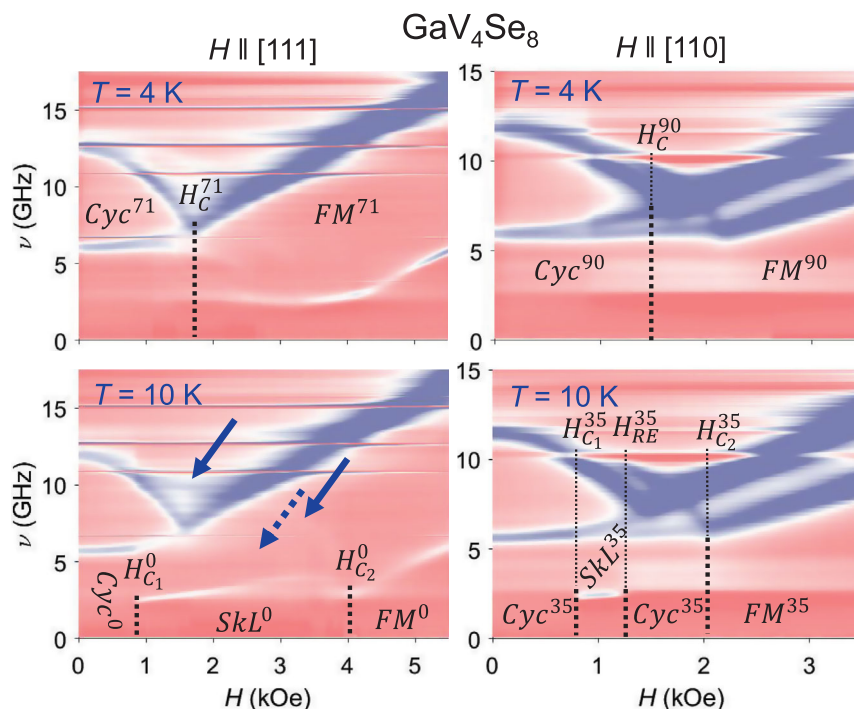


Figure 9. Color-coded plots of the transmission spectra $|S_{12}|$ of GaV_4Se_8 in the frequency versus magnetic field plane at temperatures of 4 and 10 K for the static field applied along the cubic [111] direction (left frames) and [110] direction (right frames), red: zero level, blue: strong absorption. Horizontal features are attributed to resonances in the CPW and cables. The magnetic phases and corresponding transitions for the different crystallographic domains characterized by their orientation (0° , 35° , 71° , and 90°) with respect to the external magnetic field are explained in the text.

2.5 GHz represents one of the three characteristic modes of the SkL. Looking closer to the data, one recognizes a second mode of the SkL phase which separates from the upper mode of the Cyc phase close to H_{C1}^0 with a frequency of ≈ 10 GHz (cf. solid arrows). This second mode crosses the FMR of the three other domains and appears again above 2.5 kOe at 8 GHz. To higher fields, it is bent further down towards the mode at 2.5 GHz. The existence of a third mode (cf. dotted arrow) is suggested by a weak absorption appearing at about 6 GHz above H_C^{71} between the other two SkL modes.

For $H||[110]$, the two domains with their hard axis perpendicular to the field show only the Cyc to FM transition at $H_C^{90} \approx 1.5$ kOe with the unification of the two Cyc modes into one FMR line, as depicted on the right-hand side of Figure 9. However, for those domains with the hard axis spanning an angle of 35.3° , the appearance of the resonance line at 2.5 GHz between $H_{C1}^{35} \approx 0.8$ kOe and $H_{RE}^{35} \approx 1.2$ kOe establishes the onset of the SkL phase and reentrance of the Cyc phase before its transition into the FM phase at about $H_{C2}^{35} \approx 2.1$ kOe. Due to the increase in the anisotropy on decreasing temperature the SkL phase and re-entrance to the Cyc phase is only observable at intermediate temperatures but disappears below 7 K.^[28,29] For a future detailed investigation of the SkL modes, it will be necessary to prepare a single-domain crystal by poling the sample in strong external fields during cooling through the Jahn–Teller transition.^[29]

6. Conclusion

We have discussed NMR and ESR data of the lacunar spinels GaV_4S_8 and GaV_4Se_8 . NMR turned out to be very sensitive to structural distortions due to the Jahn–Teller effect. The splitting of the spectra due to the interaction between the nuclear quadrupole moment and surrounding charges serves as a local measure of the dielectric polarization, whereas the line shift of the spectra probes the local magnetic susceptibility. The eigenmodes of the collective excitations have been experimentally detected by broadband ESR technique and theoretically calculated for all magnetic phases of GaV_4S_8 with easy-axis magnetic anisotropy. In the Cyc phase, the basic splitting of the eigenmodes arises from the uniaxial anisotropy of the rhombohedrally distorted domains. In the Néel-type SkL phase, CW, CCW, and BR modes have been identified and a further splitting of the CW mode was established in oblique magnetic fields. Our first results of broadband ESR measurements in the easy-plane compound GaV_4Se_8 reveal the broad SkL regime for the domain with its rhombohedral axis aligned parallel to the magnetic field and a strong orientation dependence of the SkL phase with respect to the magnetic field. Further theoretical considerations including the anisotropy of g values and demagnetization due to sample shape are necessary to understand all details of resonance shifts and intensities of the observed ESR spectra.

Acknowledgements

The authors acknowledge financial support by the Deutsche Forschungsgemeinschaft (DFG) via the Transregional Research Center TRR 80 "From Electronic Correlations to Functionality", project no. 107745057 (Augsburg, München, Stuttgart). The authors highly appreciate useful discussions with A. Loidl and are grateful for his support.

Open access funding enabled and organized by Projekt DEAL.

Conflict of Interest

The authors declare no conflict of interest.

Data Availability Statement

The data that support the findings of this study are available from the corresponding author upon reasonable request.

Keywords

electron spin resonance, lacunar spinels, nuclear magnetic resonance

Received: April 22, 2021

Revised: October 12, 2021

Published online:

-
- [1] P. G. Radaelli, D. E. Cox, M. Marezio, S.-W. Cheong, *Phys. Rev. B* **1997**, *55*, 3015.
- [2] S. Schaile, H.-A. Krug von Nidda, J. Deisenhofer, A. Loidl, T. Nakajima, Y. Ueda, *Phys. Rev. B* **2012**, *85*, 205121.
- [3] M. Lohmann, H.-A. Krug von Nidda, M. V. Eremin, A. Loidl, G. Obermeier, S. Horn, *Phys. Rev. Lett.* **2000**, *85*, 1742.
- [4] M. Heinrich, H.-A. Krug von Nidda, R. M. Eremina, A. Loidl, Ch. Helbig, G. Obermeier, S. Horn, *Phys. Rev. Lett.* **2004**, *93*, 116402.
- [5] S. Kondo, D. C. Johnston, C. A. Swenson, F. Borsa, A. V. Mahajan, L. L. Miller, T. Gu, A. I. Goldman, M. B. Maple, D. A. Gajewski, E. J. Freeman, N. R. Dilley, R. P. Dickey, J. Merrin, K. Kojima, G. M. Luke, Y. J. Uemura, O. Chmaissem, J. D. Jorgensen, *Phys. Rev. Lett.* **1997**, *78*, 3729.
- [6] H. Kaps, M. Brando, W. Trinkl, N. Büttgen, A. Loidl, E.-W. Scheidt, M. Klemm, S. Horn, *J. Phys.: Condens. Matter* **2001**, *13*, 8497.
- [7] T. Dey, M. Majumder, J. C. Orain, A. Senyshyn, M. Prinz-Zwick, S. Bachus, Y. Tokiwa, F. Bert, P. Khuntia, N. Büttgen, A. A. Tsirlin, P. Gegenwart, *Phys. Rev. B* **2017**, *96*, 174411.
- [8] A. Revelli, M. Moretti Sala, G. Monaco, P. Becker, L. Bohatý, M. Hermanns, T. C. Koethe, T. Fröhlich, P. Warzanowski, T. Lorenz, S. V. Streltsov, P. H. M. van Loosdrecht, D. I. Khomskii, J. van den Brink, M. Grüninger, *Sci. Adv.* **2019**, *5*, 4020.
- [9] J. P. Attfield, *APL Mater.* **2015**, *3*, 041510.
- [10] D. Johrendt, *Z. Anorg. Allg. Chem.* **1998**, *624*, 952.
- [11] I. Kézsmárki, S. Bordács, P. Milde, E. Neuber, L. M. Eng, J. S. White, H. M. Rønnow, C. D. Dewhurst, M. Mochizuki, K. Yanai, H. Nakamura, D. Ehlers, V. Tsurkan, A. Loidl, *Nat. Mater.* **2015**, *14*, 1116.
- [12] E. Ruff, S. Widmann, P. Lunkenheimer, V. Tsurkan, S. Bordács, I. Kézsmárki, A. Loidl, *Sci. Adv.* **2015**, *1*, 1500916.
- [13] S. Bordács, A. Butykai, B. G. Szigeti, J. S. White, R. Cubitt, A. O. Leonov, S. Widmann, D. Ehlers, H.-A. Krug von Nidda, V. Tsurkan, A. Loidl, I. Kézsmárki, *Sci. Rep.* **2017**, *7*, 7584.
- [14] Y. Fujima, N. Abe, Y. Tokunaga, T. Arima, *Phys. Rev. B* **2017**, *95*, 180410(R).
- [15] K. J. A. Franke, B. M. Huddart, T. J. Hicken, F. Xiao, S. J. Blundell, F. L. Pratt, M. Crisanti, J. Barker, S. J. Clark, A. Stefancic, M. Ciomaga Hatnean, G. Balakrishnan, T. Lancaster, *Phys. Rev. B* **2018**, *98*, 054428.
- [16] Ke Xu, H. J. Xiang, *Phys. Rev. B* **2015**, *92*, 121112(R).
- [17] E. Neuber, P. Milde, A. Butykai, S. Bordács, H. Nakamura, T. Waki, Y. Tabata, K. Geirhos, P. Lunkenheimer, I. Kézsmárki, *J. Phys.: Condens. Matter* **2018**, *30*, 445402.
- [18] H. Ishikawa, T. Yajima, A. Matsuo, Y. Ihara, K. Kindo, *Phys. Rev. Lett.* **2020**, *124*, 227202.
- [19] K. Geirhos, J. Langmann, L. Prodan, A. A. Tsirlin, A. Missiul, G. Eickerling, A. Jesche, V. Tsurkan, P. Lunkenheimer, W. Scherer, I. Kézsmárki, *Phys. Rev. Lett.* **2021**, *126*, 187601
- [20] S. Seki, X. Z. Yu, S. Ishiwata, Y. Tokura, *Science* **2012**, *336*, 198.
- [21] O. Janson, I. Rousochatzakis, A. A. Tsirlin, M. Belesi, A. A. Leonov, U. K. Rössler, J. van den Brink, H. Rosner, *Nat. Commun.* **2014**, *5*, 5376.
- [22] L. Hozoi, M. S. Eldeeb, U. K. Rößler, *Phys. Rev. Res.* **2020**, *2*, 022017(R).
- [23] S. Reschke, F. Meggle, F. Mayr, V. Tsurkan, L. Prodan, H. Nakamura, J. Deisenhofer, C. A. Kuntscher, I. Kézsmárki, *Phys. Rev. B* **2020**, *101*, 075118.
- [24] D. Ehlers, I. Stasinopoulos, I. Kézsmárki, T. Fehér, V. Tsurkan, H.-A. Krug von Nidda, D. Grundler, A. Loidl, *J. Phys.: Condens. Matter* **2017**, *29*, 065803.
- [25] D. Ehlers, I. Stasinopoulos, V. Tsurkan, H.-A. Krug von Nidda, T. Fehér, A. Leonov, I. Kézsmárki, D. Grundler, A. Loidl, *Phys. Rev. B* **2016**, *94*, 014406.
- [26] S. Widmann, E. Ruff, A. Günther, H.-A. Krug von Nidda, P. Lunkenheimer, V. Tsurkan, S. Bordács, I. Kézsmárki, A. Loidl, *Philos. Mag.* **2017**, *97*, 3428.
- [27] E. Ruff, A. Butykai, K. Geirhos, S. Widmann, V. Tsurkan, E. Stefanet, I. Kézsmárki, A. Loidl, P. Lunkenheimer, *Phys. Rev. B* **2017**, *96*, 165119.
- [28] A. O. Leonov, I. Kézsmárki, *Phys. Rev. B* **2017**, *96*, 214413.
- [29] K. Geirhos, B. Gross, B. G. Szigeti, A. Mehlin, S. Philipp, J. S. White, R. Cubitt, S. Widmann, S. Ghara, P. Lunkenheimer, V. Tsurkan, E. Neuber, D. Ivaneyko, P. Milde, L. M. Eng, A. O. Leonov, S. Bordács, M. Poggio, I. Kézsmárki, *Nat. Quantum Mater.* **2020**, *5*, 44.
- [30] J. Seliger, V. Zagar, T. Asaji, K. Gotohe, H. Ishida, *Phys. Chem. Chem. Phys.* **2011**, *13*, 9165.
- [31] A. M. Clogston, V. Jaccarino, *Phys. Rev.* **1961**, *121*, 1357.
- [32] T. Schwarze, J. Waizner, M. Garst, A. Bauer, I. Stasinopoulos, H. Berger, C. Pfleiderer, D. Grundler, *Nat. Mater.* **2015**, *14*, 478.
- [33] I. Stasinopoulos, S. Weichselbaumer, A. Bauer, J. Waizner, H. Berger, M. Garst, C. Pfleiderer, D. Grundler, *Sci. Rep.* **2017**, *7*, 7037.
- [34] R. Keesman, A. O. Leonov, P. van Dieten, S. Buhandt, G. T. Barkema, L. Fritz, R. A. Duine, *Phys. Rev. B* **2015**, *92*, 134405.
- [35] M. Mochizuki, *Phys. Rev. Lett.* **2012**, *108*, 017601.
- [36] Y. Wiemann, J. Simmendinger, C. Clauss, L. Bogani, D. Bothner, D. Koelle, R. Kleiner, M. Dressel, M. Scheffler, *Appl. Phys. Lett.* **2015**, *106*, 193505.
- [37] A. G. Gurevich, G. A. Melkov, *Magnetization Oscillations and Waves*, CRC Press, Boca Raton, FL **1996**.